

Appendix C

**Application of Hydrodynamic and Sediment Transport
Models for Cleanup Efforts Related to the Deepwater
Horizon Oil Spill Along the Coast of Mississippi and
Louisiana**

**Prepared in cooperation with the Operational Science Advisory Team (OSAT3) Steering
Committee chartered by the Deepwater Horizon Federal On-Scene Coordinator (FOSC)**

By Ioannis Y. Georgiou, Zoe J. Hughes, Kevin Trosclair

May 20, 2013

Table of Contents

List of Figures	4
List of Tables.....	6
Application of Hydrodynamic and Sediment Transport Models for Cleanup Efforts Related to the Deepwater Horizon Oil Spill Along the Coast of Mississippi and Louisiana	7
Introduction.....	7
Overall OSAT3 Objectives	7
Objectives of the Hydrodynamic and Sediment Transport Models	8
Methods.....	9
Modeling Approach and Theory	10
Hydrodynamic Model Description.....	12
Hydrodynamic Model Input Data	19
Bathymetry	19
Waves	19
Winds.....	20
SRB and Sand Movement	20
Metrics for Evaluating Sand and SRB Mobility and Redistribution Patterns.....	21
Significant Wave Height	22
Alongshore rms-current Convergences	22
Weighted Mobility Probability.....	22
Tidal Mobility.....	23
Results.....	23
Model Evaluation	27
Tidal Model – Barataria Basin.....	27
Tidal Models – Pontchartrain, Mississippi and Breton Sound	29

Wave Model	36
Summary and Concluding remarks	37
References	38

List of Figures

Figure 1 Computational grids for Wave modeling using SWAN; Black are the regional grids, and green and white, show the location and extent of the nested grids. Regional grid resolution is 500 m, while nested grid resolution is 100 m in LA and 75 m in MS. Also shown are the locations of the NOAA buoy 42040, and CSI locations where additional data for model skill were used.....	10
Figure 2 Wave analysis to determined wave statistics used in numerical wave modeling; five magnitude bins, and 16 directions were considered (80 scenarios); ignoring offshore winds, the simulation matrix was reduced to 40 scenarios.	11
Figure 3 Model computational domain with varying resolution from over 2 Km near the open boundary to 40 m in tidal passes and waterways. Only wet elements are shown, while the red boundary indicates the entire domain.	14
Figure 4 Computational grid domain mesh from southeast Louisiana to the Florida/Alabama state line (coordinates in UTM 15, meters).....	15
Figure 5 Results from significant wave heights (top panel) and mobility and transport (kg/m/s - bottom panel) for SRB class 1 resulting from scenario 37 which includes winds from the southwest. Wave direction is shown with vectors while magnitude of wave height and transport is shown with contours.	24
Figure 6 Results from significant wave heights (top panel) and mobility and transport (kg/m/s - bottom panel) for SRB class 1 resulting from scenario 40 which includes winds from the west. Wave direction is shown with vectors while magnitude of wave height and transport is shown with contours.....	25
Figure 7 Results from significant wave heights (top panel) and mobility and transport (kg/m/s - bottom panel) for sand resulting from scenario 40 which includes winds from the west. Wave direction is shown with vectors while magnitude of wave height and transport is shown with contours.	26
Figure 8 Graphical comparison of model simulated constituents with observations obtained from harmonic analysis during the validation period for August 2007.....	29
Figure 9 The inset shows a map of the states surrounding the northern Gulf of Mexico, while the red box outlines the area shown in the large image. The large image is a map of the calibration stations within the domain. Table 3 describes these stations in more	31

Figure 10 - Meteorological conditions at the NOAA NOS Gulfport Outer Range station (Station GPOM6 – 8744707) for the period of 3/31/10 to 5/7/10. 32

Figure 11 – Comparison of base-case scenario tides (meters) and observed tide data for the calibration period (3/31/10 to 4/22/10). Calibration efforts focused on good correlation during the period of 4/16/10 to 4/22/10 (inside the green box) at the following locations (from top to bottom): Lake Pontchartrain at LUMCON, Rigolets near Lake Pontchartrain, and Mississippi Sound at St. Joseph Island Light. An adjustment was applied to observed data to account for vertical datum differences. 33

Figure 12 - Comparison of base-case scenario tides (meters) and observed tide data for the calibration period (3/31/10 to 4/22/10). Calibration efforts focused on good correlation during the period of 4/16/10 to 4/22/10 (inside the green box) at the locations (from top to bottom): D2, NE Bay Gardene near Point à la Hache and Barataria Pass at Grand Isle. An adjustment was applied to observed data to account for vertical datum differences. 34

Figure 13 Wave model skill showing significant wave height comparison at station CSI 9..... 37

Figure 14 Wave model skill showing significant wave height comparison at station CSI 16..... 37

List of Tables

Table 1 Additional scenarios simulated to represent storm conditions	12
Table 2 Critical velocity used in Sediment transport and SRB mobility calculations.....	19
Table 3 Size classes for natural sediment and SRBs used in the study, with corresponding density, and critical velocities.....	21
Table 4 Observed and simulated tidal constituents during model validation (values are in meters)	28
Table 5 - Stations used for model calibration. Station name, number, and operating agency, as well as calibration parameter are provided. Station numbers are in parentheses after station name.....	31
Table 6 – MAE and RMSE values (in meters) at each tidal calibration station during the period of 4/16/10 to 4/22/10. Stations are shown in ascending order of error.....	36

Application of Hydrodynamic and Sediment Transport Models for Cleanup Efforts Related to the Deepwater Horizon Oil Spill Along the Coast of Mississippi and Louisiana

By Ioannis Y. Georgiou, Zoe Hughes and Kevin Trosclair

Introduction

Residual oil from the Deepwater Horizon spill is found in the shallow surf-zone in the northern Gulf of Mexico in two primary forms: submerged oil mats and surface residual balls (SRBs). Mats formed when weathered oil at the surface reached either a shallow environment with sufficient mixing to facilitate entrainment of sand into the water column to mix with the oil, and therefore settle, or when surface oil arriving near coastlines was stranded and seeped into the sand at low tide. Mats encountered as part of the Deepwater Horizon response efforts are generally meters in cross-shore width, meters to tens of meters in alongshore length, and a few to tens of centimeters thick. Under high energy events such as winter storms and extratropical systems, buried mats can be exhumed and pieces of the mats can break off and form SRBs (Shoreline Cleanup and Assessment Team, oral commun., 2012). The SRBs are observed in the surf zone and may wash up on beaches. SRBs and mats in the surf zone and on the beach are targets of ongoing cleanup response efforts. This report presents the results of a subgroup that developed hydrodynamic and sediment transport models and developed techniques for analyzing potential SRB redistribution and burial and exhumation to provide a better understanding of alongshore processes and movement of SRBs along the coastline of Mississippi and Louisiana.

Overall OSAT3 Objectives

To provide improved understanding and guidance in support of the operational response to shoreline re-oiling, Operational Science Advisory Team (OSAT3) undertook five main tasks:

- Evaluate the trends observed in frequency, rate, and potential for remobilization on beach segments in the areas affected by re-oiling.

- Determine and record the locations and typical shoreline profiles and morphology for likely sources of residual oil or origin of the SRBs.
- Define or determine the mechanisms whereby re-oiling phenomena may be occurring.
- Investigate the potential for mitigation actions that may be taken to reduce these potential occurrences and, evaluate the feasibility of the mitigation actions and net environmental benefit.
- Recommend a path forward to reach shoreline cleanup completion plan guidelines or appropriately manage identified areas through alternative methods.

To achieve these overall objectives, the OSAT3 team collected and analyzed shoreline cleanup data (for example, SRB and mat recovery, high resolution stereoscopic images) and geomorphic data (beach profiles, aerial imagery, shorelines, topography, and bathymetry) and conducted numerical modeling analysis of waves, water levels, currents, local surficial sediment, and SRB mobility and transport. This report specifically addresses the numerical modeling aspect of the OSAT3 objectives along the coastline of Louisiana and Mississippi; overall OSAT3 findings are not within the scope of the analysis of this report.

Objectives of the Hydrodynamic and Sediment Transport Models

This report documents the approach, results, and discussion from the LA/MS OSAT3 subgroup (hereafter LAMS-O3) that developed hydrodynamic and sediment (including SRBs) transport models to provide better understanding and prediction of alongshore processes and movement of SRBs. This report addresses the work for Louisiana and Mississippi coastlines. The specific objectives of this subgroup's effort were to

- identify spatial patterns in alongshore current directions and velocity

- identify zones of convergence and alongshore current reversal
- identify potential sediment and SRB sinks
- estimate SRB movement along the coast
- determine the influence of tidal currents on SRB mobility and transport in the vicinity of tidal inlets (where needed)

These objectives were achieved through modeling scenarios covering the range of weather and wave variability since the Deepwater Horizon spill; extracting alongshore root-mean-square (rms) currents, wave-orbital stirring, and tidal currents; and computing associated sediment and SRB mobility and alongshore transport patterns (magnitude and direction).

Methods

The coastline of interest included in this analysis covers the barrier island in coastal Louisiana stretches from west Isles Dernieres Louisiana, to Mobile Inlet, Alabama. The domain of interest and focus however, is on the barrier islands of Mississippi, mainland Mississippi, and the entire coastline of Louisiana from Isles Dernieres to Pelican Island. We utilized a combination of unstructured grids for the tidal models and Cartesian grids for the Wave models, and followed a nested approach, whereby regional processes are modeled at lower resolution, and local – nearshore – processes are simulated at higher resolution. Tidal model resolution varies from 10s of meters near coastlines to 10 km at the open boundary in the Gulf of Mexico, and wave model resolution is constant at 500 m offshore, with nested local grids with 75 - 100 m resolution (Figure 1). The nearshore grids were oriented at an angle parallel to the local shoreline angle for simplicity, and to avoid stair-stepping effects.

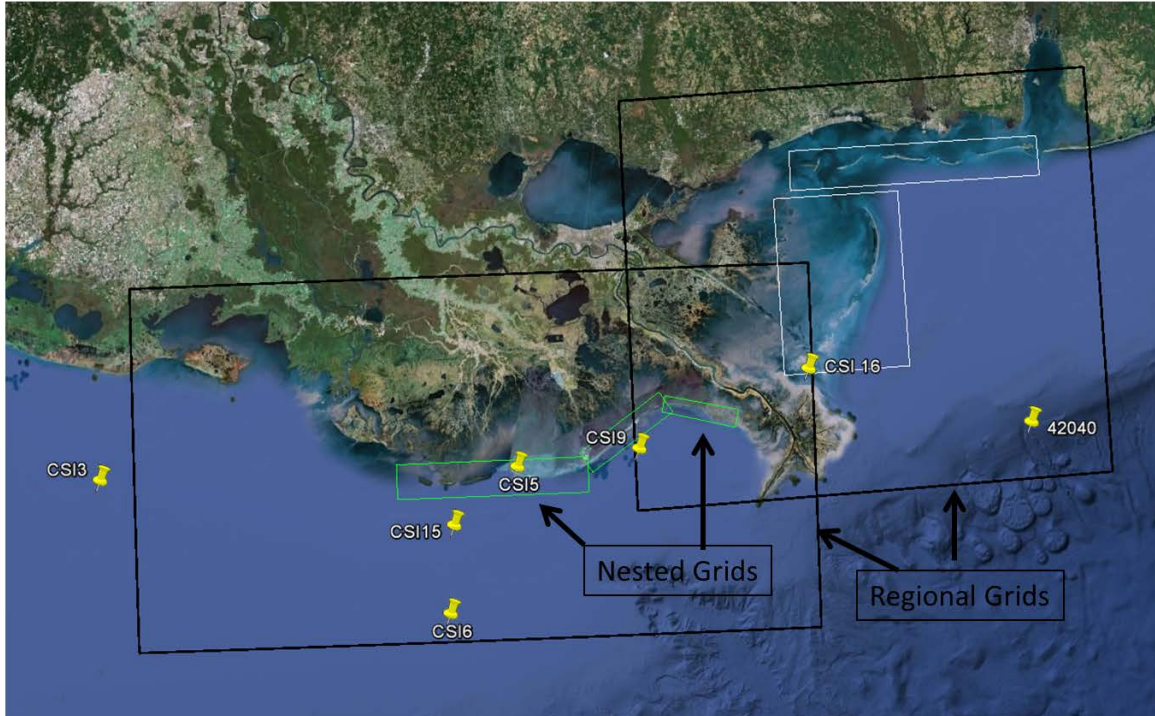


Figure 1 Computational grids for Wave modeling using SWAN; Black are the regional grids, and green and white, show the location and extent of the nested grids. Regional grid resolution is 500 m, while nested grid resolution is 100 m in LA and 75 m in MS. Also shown are the locations of the NOAA buoy 42040, and CSI locations where additional data for model skill were used.

Modeling Approach and Theory

Hydrodynamic simulations included scenarios derived from wave and weather observations at the National Oceanic and Atmospheric Administration (NOAA) buoy 42040 from April 1, 2010, to August 1, 2012. This analysis was conducted by the eastern states subgroup lead by Nathaniel Plant, USGS. The buoy is located near the offshore boundary of the regional domain, and is therefore appropriate to use as offshore boundary condition. The wave observations were schematized by dividing wave heights into 5 bins bounded by 0.0, 0.5, 1.0, 1.5, 2.0, and 5.0 m and sampling wave directions in 16 bins each spanning 22.5 degrees ($^{\circ}$), from 0° to 360° . The combination of wave height and direction bins yielded 80 different scenarios. Offshore winds were ignored, leaving 40 remaining scenarios for simulations. Additionally, 7 scenarios were added, representing a typical winter storm (post-frontal), and the 1-yr, 10-yr, and 100-yr storm waves, approaching from two dominant directions (Figure 2), and a 1-yr, 10-yr, and 100-yr storm

wave at the open boundary, approaching from two directions. This analysis was performed using data from the same buoy (NOAA, 42040) but utilizing a record of 11 years, and the Peak-over-threshold (POT) approach (Table 1).

We applied a constant wave along the open boundary. Although a rather large geographic extend, the segmentation of the regional grids into two domains, the large distance of the offshore boundary away from the shore and area of interest, along with the low gradient continental shelf, parallel bathymetric contours, and low surfzone slope, all contribute to this assumption and methodology being appropriate. Tests showed that nearshore waves in Louisiana are unaffected by variable wave climate at the open boundary, hence a constant wave boundary condition was used.

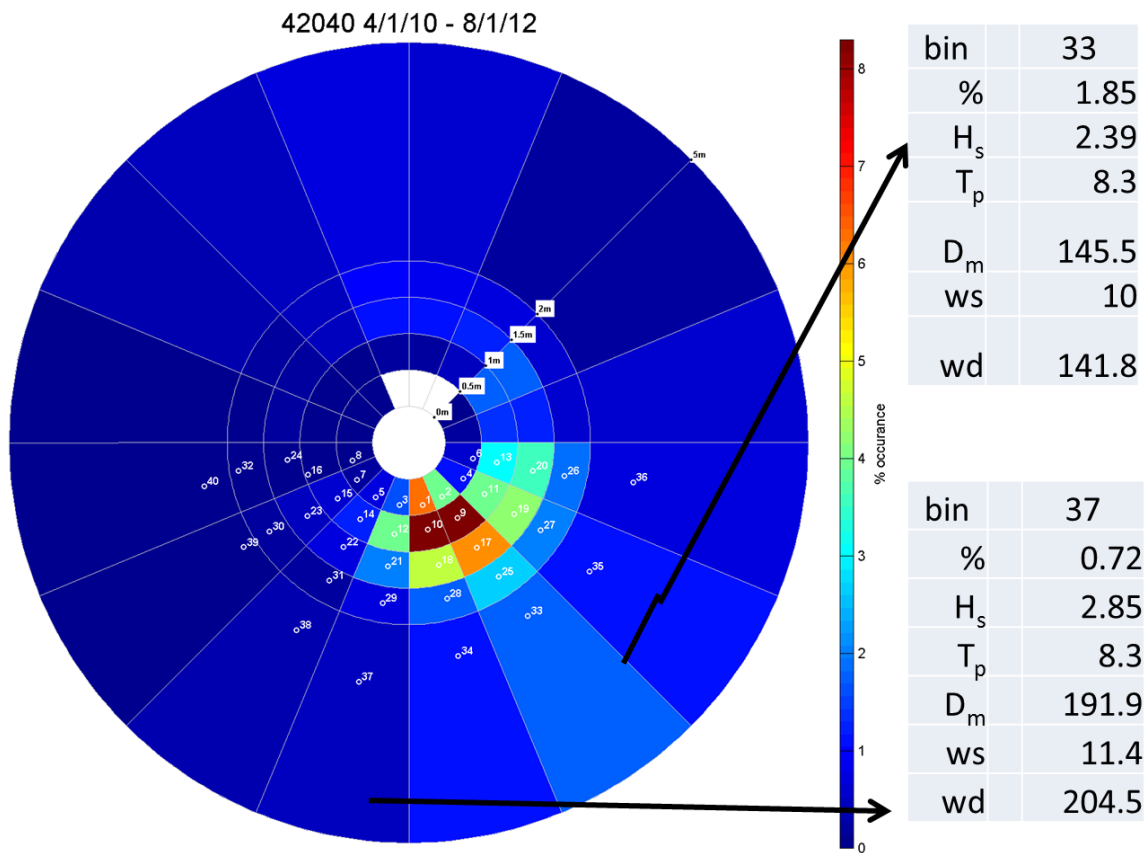


Figure 2 Wave analysis to determined wave statistics used in numerical wave modeling; five magnitude bins, and 16 directions were considered (80 scenarios); ignoring offshore winds, the simulation matrix was reduced to 40 scenarios.

Table 1 Additional scenarios simulated to represent storm conditions

Run	Water level (m)	Hs (m)	Tp (s)	Direction	Wind Speed (m/s)	Wind direction
41	4	20	17	135	42	135
42	4	20	17	180	42	180
43	3	14	13.5	135	28	135
44	3	14	13.5	180	28	180
45	1.5	6.5	9	135	19	135
46	1.5	6.5	9	180	19	180
47	0	0	0	315	10	315

Hydrodynamic Model Description

We used the Finite Volume Coastal Ocean Model (FVCOM) version 2.7 (Chen et al., 2003), which is a prognostic, unstructured-grid, finite-volume, free-surface, 3-D primitive equation coastal ocean circulation model developed by Chen et al., (2003). The model consists of momentum, continuity, temperature, salinity, and density equations and is closed physically and mathematically using turbulence closure sub-models (Mellor and Yamada, 1982; Burchard, 2002). The horizontal grid is composed of unstructured triangular cells, and the irregular bottom is represented using generalized terrain-following coordinates (otherwise known as sigma coordinates). The General Ocean Turbulent Model (GOTM) developed by Burchard (2002) has been added to FVCOM to provide optional vertical turbulent closure schemes. FVCOM is solved numerically by a second-order accurate, discrete flux calculation in the integral form of the governing equations over an unstructured triangular grid. This approach combines the best features of finite-element methods (grid flexibility) and finite-difference methods (numerical efficiency and code simplicity) and provides a much better numerical representation of both local and global momentum, mass, salt, heat, and tracer conservation. The equations for momentum, continuity, temperature, salinity, and density are as follows:

$$\frac{\partial u}{\partial t} + u \frac{\partial u}{\partial x} + v \frac{\partial u}{\partial y} + w \frac{\partial u}{\partial z} - fv = -\frac{1}{\rho_0} \frac{\partial P}{\partial x} + \frac{\partial}{\partial z} \left(K_m \frac{\partial u}{\partial z} \right) + F_u \quad (1)$$

$$\frac{\partial v}{\partial t} + u \frac{\partial v}{\partial x} + v \frac{\partial v}{\partial y} + w \frac{\partial v}{\partial z} + fu = -\frac{1}{\rho_0} \frac{\partial P}{\partial y} + \frac{\partial}{\partial z} \left(K_m \frac{\partial v}{\partial z} \right) + F_v \quad (2)$$

$$\frac{\partial P}{\partial z} = -\rho g \quad (3)$$

$$\frac{\partial u}{\partial x} + \frac{\partial v}{\partial y} + \frac{\partial w}{\partial z} = 0 \quad (4)$$

$$\frac{\partial \theta}{\partial t} + u \frac{\partial \theta}{\partial x} + v \frac{\partial \theta}{\partial y} + w \frac{\partial \theta}{\partial z} = \frac{\partial}{\partial z} \left(K_h \frac{\partial \theta}{\partial z} \right) + F_\theta \quad (5)$$

$$\frac{\partial s}{\partial t} + u \frac{\partial s}{\partial x} + v \frac{\partial s}{\partial y} + w \frac{\partial s}{\partial z} = \frac{\partial}{\partial z} \left(K_h \frac{\partial s}{\partial z} \right) + F_s \quad (6)$$

$$\rho = \rho(\theta, s) \quad (7)$$

where x , y , and z are the east, north, and vertical axes of the Cartesian coordinate; u , v , and w are the x , y , and z velocity components; θ is the potential temperature; s is the salinity; ρ is the density; P is the pressure; f is the Coriolis parameter; g is the gravitational acceleration; K_m is the vertical eddy viscosity coefficient; and K_h is the thermal vertical eddy diffusion coefficient. Here F_u , F_v , and F_s represent the horizontal momentum, thermal and salt diffusion terms. For a more detailed description of model development and other capabilities the reader is directed to Chen et al., (2003). The model has been used previously in three-dimensional mode due to the episodic

and seasonal stratification that the estuary experiences (Poirrier, 1979; Li et al, 2008; Georgiou et al, 2009) and to capture additional stratification potentially induced near freshwater input sources. The freely available source code for FVCOM does not readily offer salinity transport under the two-dimensional mode without code modifications.

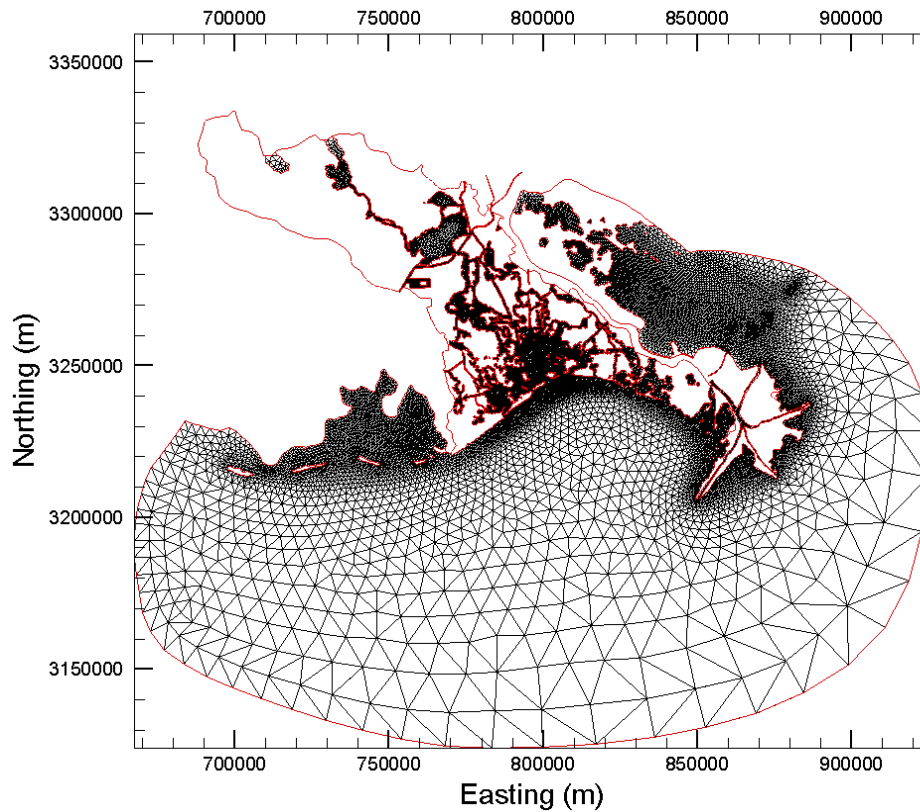


Figure 3 Model computational domain with varying resolution from over 2 Km near the open boundary to 40 m in tidal passes and waterways. Only wet elements are shown, while the red boundary indicates the entire domain.

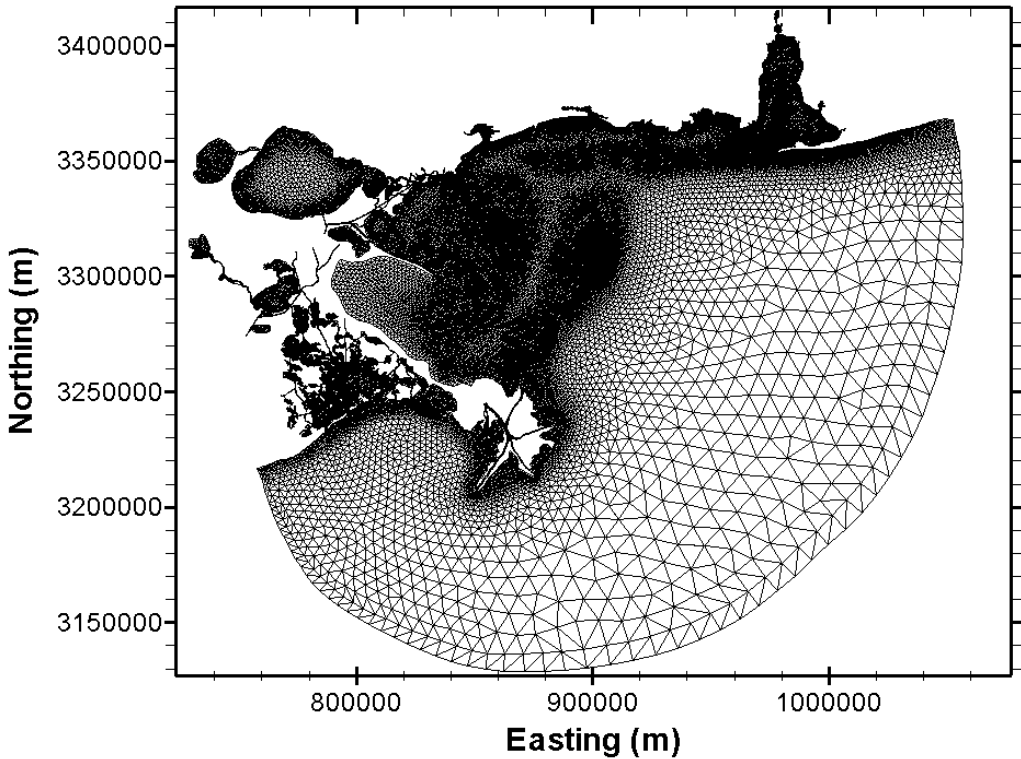


Figure 4 Computational grid domain mesh from southeast Louisiana to the Florida/Alabama state line (coordinates in UTM 15, meters).

For waves we used the Simulating WAVes in the Nearshore (SWAN) model, a third-generation wave model, developed at Delft University of Technology, that computes random, short-crested wind-generated waves in coastal regions and inland waters. The SWAN model can account for the following physics:

- Wave propagation in time and space, shoaling, refraction due to current and depth, frequency shifting due to currents and non-stationary depth.
- Wave generation by wind.
- Three- and four-wave interactions.
- Whitecapping, bottom friction and depth-induced breaking.
- Dissipation due to vegetation.
- Wave-induced set-up.
- Propagation from laboratory up to global scales.
- Transmission through and reflection (specular and diffuse) against obstacles.
-

Three-dimensional surf zone processes were not simulated due to the focus on the prediction and role of alongshore currents (as opposed to cross-shore processes) in transporting SRBs along the domain for the project. The results of the model show that the nearshore is dominated by wave breaking processes and vertical profiles of wave-driven alongshore currents have been observed to be relatively depth uniform (Reniers et al., 2004), suggesting that the assumption, and use of a depth-integrated velocity is valid. Density stratification effects were assumed minimal and were ignored; it is assumed that intense vertical mixing by breaking waves will produce a homogenous density field. All models were also driven by winds, which were spatially constant but time-dependent – for time-dependent tidal simulations. The 47 scenario simulations for waves were run as stationary waves, i.e. there was no time-dependent component. Variable water depth and its influence on wave refraction, shoaling, and breaking and alongshore variations in the rms velocity were included, as was a reasonable estimate of density of water in a marine setting.

Alongshore rms current directions and magnitudes (for example, eastward or westward following the curvature of the model grid) were required to understand the movement of sediments and SRBs under various wave conditions. Incident waves approaching the shoreline at an angle break and transfer their momentum to the water column, creating the primary force that is responsible for driving alongshore currents (generally, waves approaching from the west drive currents to the east and vice versa). Depending on the local geometry of the coast and nearshore bathymetry, complex spatial patterns in the magnitude and direction of these current can develop. These variations can then form convergence or divergence locations (nodal points) and are of relative importance, since SRBs can accumulate or their transport be interrupted at these locales. This effort produced locations from each of the scenarios simulated where convergence or divergence points exist.

Sediment transport

To assess sediment transport and likely SRB movement alongshore, we employed a semi-empirical relationship used by Soulsby-Van Rijn. These algorithms account for transport under

both currents and waves and are summarized herein; a full treatment is available in Soulsby (1997). The mass transport, Qt (kg/s/m), is given by

$$Qt = \rho_s q_t \quad (8)$$

where ρ_s is the sediment density (2650 kg/m³), and

$$q_t = (A_s U_{avg}) \left[\sqrt{U_{avg}^2 + \frac{0.018}{C_D} U_{rms}^2} - U_{cr} \right]^{2.4} (1 - 1.6 \tan \beta) \quad (9)$$

is the volumetric transport where U_{avg} and U_{cr} are the mean and threshold current velocities (m/s), U_{rms} is the root-mean-square orbital velocity of the wave (m/s), C_D is the drag coefficient due to current alone, $\tan \beta$ is the non-dimensional bed slope, and A_s is the total load term. The total load term is given by

$$A_s = A_{sb} + A_{ss} \quad (10)$$

where A_{sb} is the bed-load term and A_{ss} is the suspended load term given by

$$A_{ss} = \frac{0.012 d_{50} D_*^{-0.6}}{[(s-1)gd_{50}]^{1.2}} \quad (11)$$

and

$$A_{sb} = \frac{0.005 h \left(\frac{d_{50}}{h}\right)^{1.2}}{[(s-1)gd_{50}]^{1.2}} \quad (12)$$

respectively, in which d_{50} is the median grain diameter (m), D_* is the dimensionless grain diameter, h is the water depth (m), g is the acceleration due to gravity (m/s²), and s is the relative density of sediment.

The current drag coefficient is calculated as

$$C_d = \left[\frac{0.4}{\ln(h/z_0) - 1} \right]^2 \quad (13)$$

with a constant bed roughness length z_0 set to 0.006 m, or $d_{50}/12$ which ever was larger.

q_t was calculated for every single point in model grid. For the nearshore shoreline vectors, we interpolated onto selected points sited just offshore (perpendicular to the shore) for clarity in viewing the results in ArcGIS.

The depth-averaged velocity was obtained from the hydrodynamic model (FVCOM), the threshold velocity (U_{cr}) was computed using Soulsby (1997), and the root-mean-square velocity (U_{rms}) was obtained from SWAN.

To determine critical velocity for movement of a selected SRB class we used the following relationships (Soulsby, 1997).

$$U_{crc} = \begin{cases} 0.19(d_{50})^{0.1} \log_{10}\left(\frac{4h}{d_{90}}\right), & \text{for } 0.1 \leq d_{50} \leq 0.5mm \\ 8.5(d_{50})^{0.6} \log_{10}\left(\frac{4h}{d_{90}}\right), & \text{for } 0.5 \leq d_{50} \leq 2.0mm \end{cases} \quad (14)$$

$$U_{crw} = \begin{cases} 0.24[(s-1)g]^{0.66} (d_{50})^{0.33} T_p^{0.33}, & \text{for } 0.1 \leq d_{50} \leq 0.5mm \\ 0.95[(s-1)g]^{0.57} (d_{50})^{0.43} T_p^{0.14}, & \text{for } 0.5 \leq d_{50} \leq 2.0mm \end{cases} \quad (15)$$

where d_{90} is the 90th percentile grain diameter, and T_p is the peak wave period. We used both equations above and selected the lowest for the sediment transport calculations. This provided for the minimum threshold for movement of each SRB class. For our 7 cases, 1 sediment and 6 SRB size classes, (assuming $h = 1.5$ m) the critical velocities are shown in the Table below.

Table 2 Critical velocity used in Sediment transport and SRB mobility calculations

SRB class	Sediment	1	2	3	4	5	6
Ucrit – currents	0.3482	0.3482	1.0272	1.3955	2.0484	2.6808	3.4206
U crit - waves	0.1942	0.1485	0.4868	0.6559	0.9726	1.3103	1.7653

Hydrodynamic Model Input Data

Bathymetry

Bathymetric data (fig. 1) were obtained from the northern Gulf Coast digital elevation map of the NOAA National Geophysical Data Center (NGDC; Love and others, 2012). These data, with 30-m resolution, satisfied the large-scale needs of the domain for the OSAT3 model. We supplemented the nearshore bathymetry in the vicinity of barrier islands in Louisiana with two supplemental datasets. One included the 2010 LiDAR dataset for the Mississippi Barrier (NOAA) and the pre-oiling bathymetry and topography around the Chandeleur Islands from 2010 (courtesy of USGS extreme storms program). Finally, using data from the Barrier Island Comprehensive Monitoring Program (BICM, Kidinger et al., 2013) we supplemented nearshore bathymetry in the central coast (Racoon to Sandy point; 2007) and topography using LiDAR from 2010, for all barriers in Louisiana where data were available (Racoon to Sandy point). More details on the availability of the bathymetric datasets in BICM can be found here (<http://pubs.usgs.gov/of/2013/1083/>).

Waves

Each of the 40 scenarios, and the additional 7 to account for larger storms, were used to force the model. Wave heights, periods, and directions were used as input to SWAN, with additional specifications which included an assumed Joint North Sea Wave Project (JONSWAP) spectral shape (Hasselmann et al., 1973). The directional domain for the wave model covered a full circle with a resolution of 10° (36 bins in total), and the frequency domain was 0.025 to 1 hertz (Hz) with logarithmic spacing. The bottom-friction dissipation parameterization of Hasselmann et al. (1973) was used with a uniform bottom roughness coefficient of 0.067 square meters per second cubed (m^2/s^3). Additionally, third-generation physics were activated, accounting for wind wave

generation, triad wave interactions, and white capping by the Komen et al. (1984) parameterization. Depth-induced wave breaking dissipation was included using the Battjes and Janssen (1978) parameterization with default values for alpha (1) and gamma (0.73).

Winds

Wind velocities were also obtained from NOAA and USGS buoys. Both tidal and wave models used wind that were constant in space – not spatially varying. For the tidal model simulations, wind velocities and directions were changing every hour during a fortnight simulation to account for the maximum tidal currents during spring tides; hence winds were time-dependent, but constant in space – i.e. the same across the domain. For the Baratavia tidal model, winds from Grand Isle were used, while for the grid covering Breton and Mississippi Sound, winds from the Grand Pass USGS station were used. These sites have long records, thus they document wind patterns more effectively and include a large number of storms in their records, and they are also positioned near open water, and hence are not influenced by land.

SRB and Sand Movement

Mobility for SRB classes was based on size and density derived from analysis of SRBs identified, analyzed and reported by the SCAT teams. The sizes identified for study in the SRB movement calculations are given in Table 3, and represent a reasonable range of what is picked up by operations. The mobility was assessed using the previously determined probability of occurrence, once the critical velocity for each scenario was exceeded (Table 3). For example, if scenario 1 represents 2 % of the typical year, if at any point in the nested grid the critical velocity was met, that cell or location was flagged with movement. This information is contained within the output files. Further, we calculated a weighted probability resulting from all 40 scenarios representing a typical year. This was conducted for the sediment class, and for each of the SRB classes. In addition to a weighted probability, we calculated weighted transport. This step is important because it separates the information provided by the weighted probability to either significant or non-significant. Although relative terms, this step will isolate an area that appears to be mobile frequently (i.e. SRBs appear to be mobile based on high probability), but exhibits a

very low mass transport rate. The following equations were used to define weighted probability and weighted mass transport rates.

$$P_w(i, j) = \sum_{k=1}^n \left(\frac{P_{k(n)}(i, j)}{P_{k(total)}} \right) \quad (16)$$

$$q_w(i, j) = \sum_{k=1}^n \left(\frac{P_{k(n)}(i, j)q_{wk}(i, j)}{P_{k(total)}} \right) \quad (17)$$

where P_w and q_w are the weighted probability and weighted transport for n scenarios, and i, j are the grid (spatial) indices.

Table 3 Size classes for natural sediment and SRBs used in the study, with corresponding density, and critical velocities

Class	Size (cm)	Density** (kg/m ³)	Critical velocity	
			(currents dominate)	(waves dominate)
Sediment (natural)	0.015*	2650	0.3482	0.1942
SRB1	0.015	2107	0.3482	0.1485
SRB2	0.5	2107	1.0272	0.4868
SRB3	1	2107	1.3955	0.6559
SRB4	2.5	2107	2.0484	0.9726
SRB5	5	2107	2.6808	1.3103
SRB6	10	2107	3.4206	1.7653

*size for natural sand class is based on local knowledge of median grain diameter

**density of SRBs was calculated using grain size data provided by British Petroleum to the USGS subgroup. Specific methodology can be found in the eastern states report.

Metrics for Evaluating Sand and SRB Mobility and Redistribution Patterns

Analyses were conducted to determine sediment and SRB movement probability and alongshore redistribution patterns for SRBs of mobilized size classes for each individual scenario,

illustrating the likely mobility and redistribution patterns under the conditions that the scenario represents. Metrics for hydrodynamics, SRB and sediment movement probability, and alongshore redistribution for wave scenarios are: significant wave height; tidal current; root-mean-square (rms) velocity produced by the wave model; and alongshore rms-current convergences and divergence. Two additional metrics used to assess the overall probability of mobility and alongshore distribution over the time period of interest, are weighted mobility probability and weighted potential mass transport rate. Metric calculations are described below.

Significant Wave Height

The significant wave height is calculated by SWAN for each scenario. This parameter is an output of the model. It is stored in the archive model output but not in the ArcGIS files.

Alongshore rms-current Convergences

The alongshore varying maximum rms-velocity computed by the SWAN wave model was used to identify flow convergences, indicating locations where the alongshore transport of SRBs would be disrupted and/or cause possible deposition zones. The rms velocity magnitude, with a sign for west-east orientation, the two components of the velocity, as well as the coordinates for convergence and divergence sites for each scenario, is stored in the ArcGIS files.

Weighted Mobility Probability

In addition to individual scenario results, the results from multiple scenarios were combined to assess persistent patterns in mobility during April 1, 2010, to August 1, 2012. For each scenario, the mobility map was converted to a binary threshold map delineating locations where the critical value for mobility had been exceeded (value = 1) and not exceeded (value = 0). For sand and each SRB class and critical threshold value, an average of this threshold exceedance map was taken and weighted by the scenario probability of occurrence over the 2-year time period being considered (Figure 2). The weighted mobility probability varies from 0 to 1, with values approaching 1 indicating mobility under most wave conditions and values approaching 0 indicating little to no mobility under any wave conditions. The weighted mobility probability is a measure of the probability that SRBs or sand are mobilized and is analogous to the fraction of time at each location that mobility occurred over the time period of interest. The mobility ratio for an individual scenario, however, as previously described, can be any number greater than or equal to 0, and is the ratio of the stress to the critical threshold value for the single point in time

represented by that scenario. The mobility ratio must exceed 1 to indicate mobility under the conditions of the scenario (see also section titled, SRB and sand movement). Spatial ArcGIS files showing the weighted mobility and weighted transport are included in a separate format in ArcGIS for each SRB class and each nested grid.

Tidal Mobility

Tidal mobility is inherent in the selection of a critical velocity. We typically selected a conservative approach to the current selection, namely those occurring during spring tides. This would provide a conservative estimate on the movement of SRBs based on tidal currents alone. However, in most cases, waves dominate the surf zone and spit platforms, especially in micro tidal settings such as Louisiana and Mississippi, and in almost all situations mobility was dominated by waves and not tidal currents.

Results

Results from all simulations (40 scenarios) were included in ESRI ArcGIS. In addition, convergence and divergent zones and weighted probability and weighted mass transport are also included. Output from the wave modeling however is also stored for the entire domain, not just along the nearshore zones. This represents gigabytes of data stored on data drives and can be submitted upon request. Example output from spatially varying parameters include among others, significant wave height, maximum wave height, period, energy dissipation terms, wave skewness, wave direction, depth, water level, bottom orbital velocity and rms-velocity.

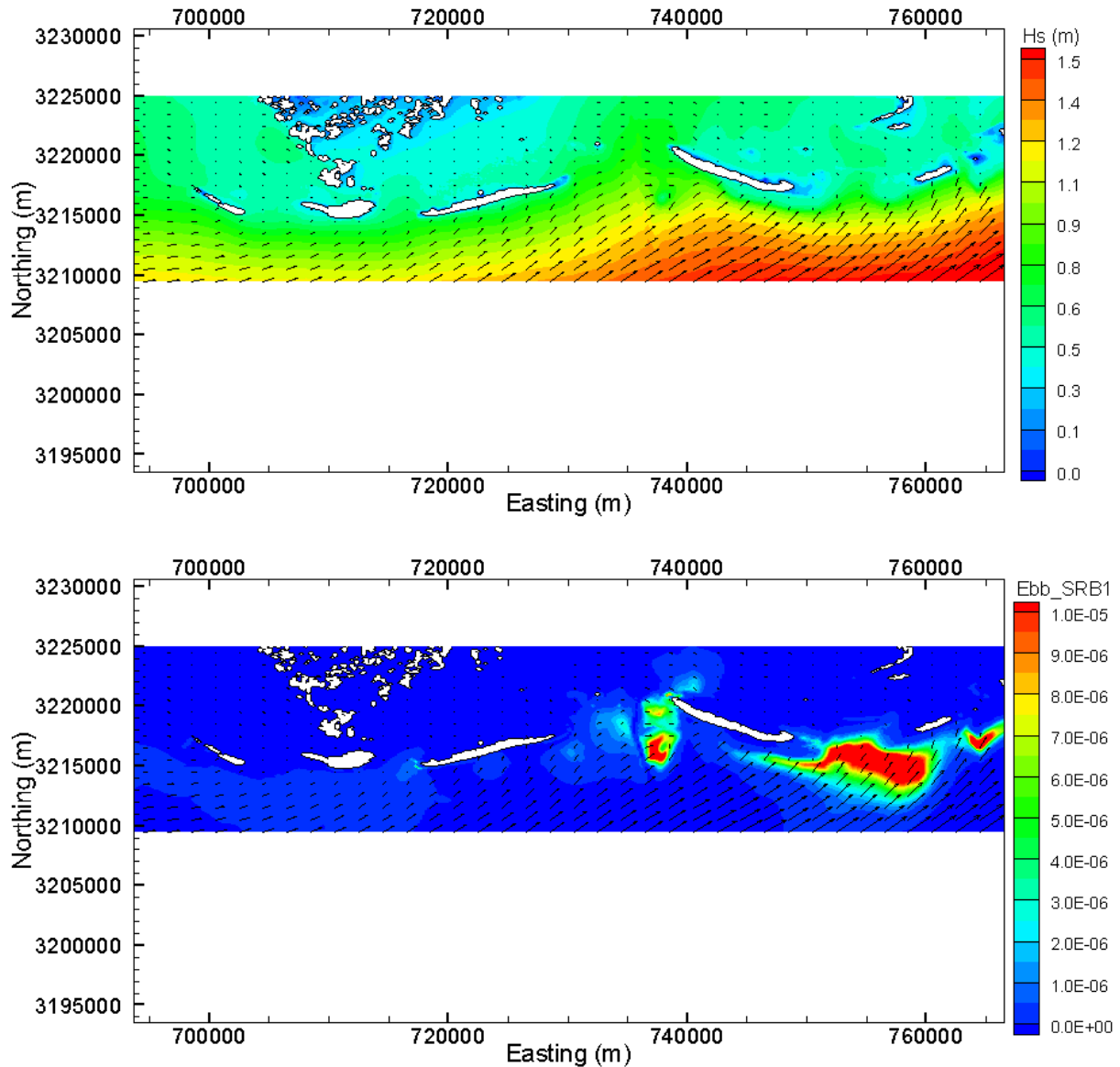


Figure 5 Results from significant wave heights (top panel) and mobility and transport (kg/m/s - bottom panel) for SRB class 1 resulting from scenario 37 which includes winds from the southwest. Wave direction is shown with vectors while magnitude of wave height and transport is shown with contours.

From the above simulation, we notice that offshore bathymetry and specifically ship shoal, located just offshore (to the south) of the area shown in (Figure 5) modifies the approaching wave energy such that wave energy arriving at the Isle Dernieres is significantly lower compared to wave energy arriving at the Timbalier chain. Subsequently, as expected, the potential for transport (Figure 5; bottom panel) appears to be much higher comparatively. Also notice that the

spit platforms, environments that are known to have active transport for longer periods appear with warm colors, suggesting that these environments do have potentially higher transport, and therefore mobility, compared to inlets and back barrier bays.

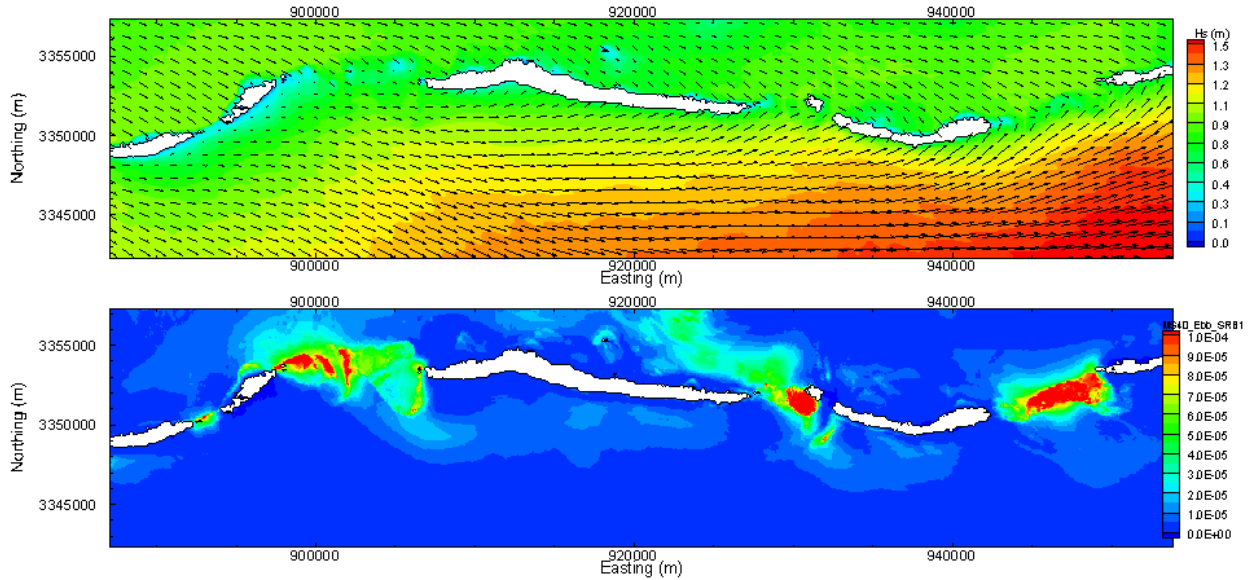


Figure 6 Results from significant wave heights (top panel) and mobility and transport (kg/m/s - bottom panel) for SRB class 1 resulting from scenario 40 which includes winds from the west. Wave direction is shown with vectors while magnitude of wave height and transport is shown with contours.

Similar to scenario 37 (southwest winds) when the islands are subject to winds from the west (high incident angle) we see evidence of waves generated in the back barrier as well as waves developing west of the Isle Dernieres barriers, which grow as they travel to the east. This is evident from the warm colors in Figure 6 (top panel), which shows waves of approximately 0.5 m growing in excess of 1.5 m across the domain (~40 km). These waves, being at high angles, transform rapidly as they encounter shallow water, seen here to create active transport zones along spit platforms. Moreover, in these simulations we see wave attack in the back barrier, generating opposing transport at downdrift locations near the island terminus.

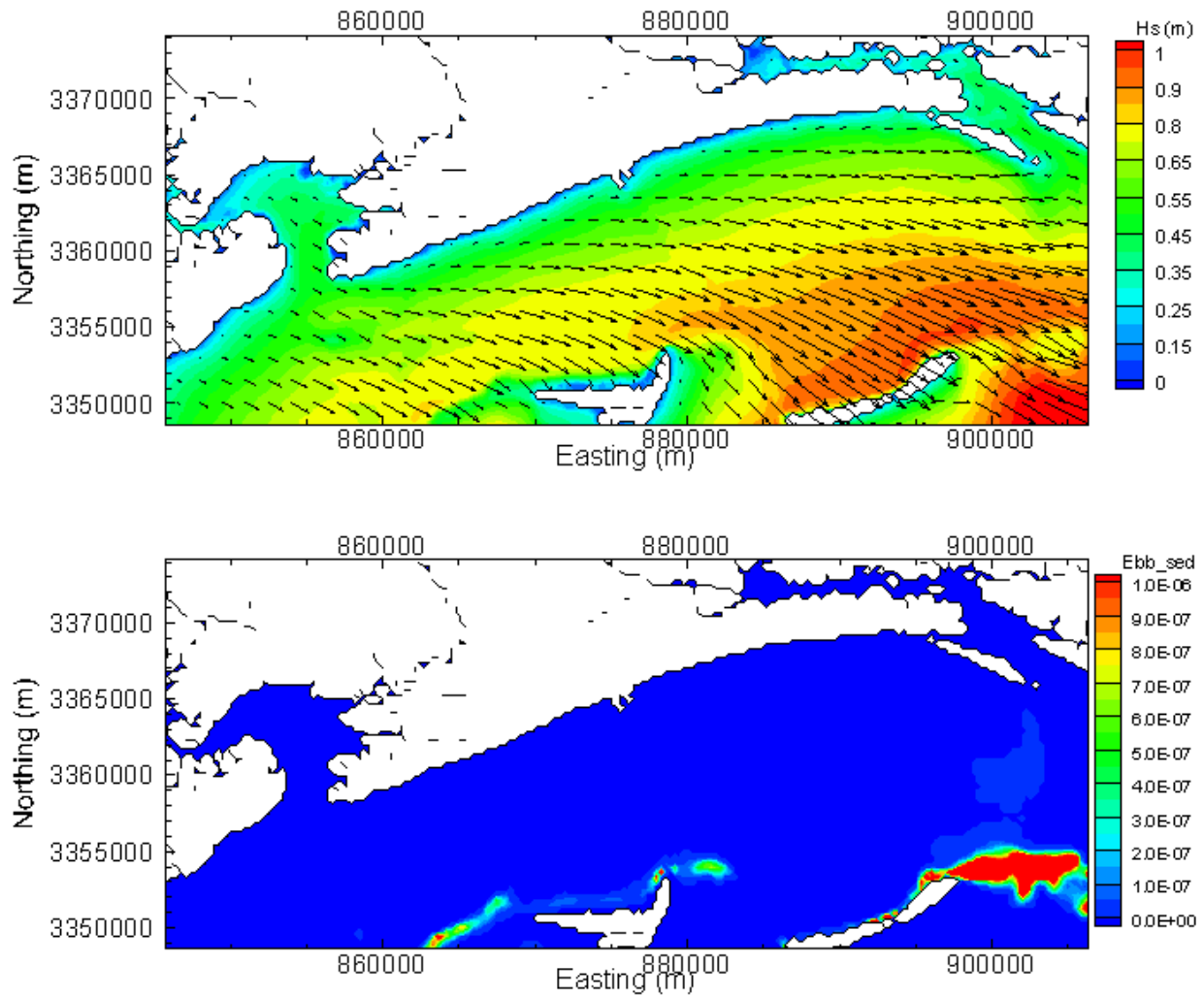


Figure 7 Results from significant wave heights (top panel) and mobility and transport (kg/m/s - bottom panel) for sand resulting from scenario 40 which includes winds from the west. Wave direction is shown with vectors while magnitude of wave height and transport is shown with contours.

Similar to west approaching winds in central Louisiana, westerly winds generate waves in Mississippi sound that grow and eventually approach the islands from the bay side. These types of conditions are typical during winter storms; in fact, post frontal winds are generally from the northwest. Figure 7 shows that waves generated in Mississippi Sound can grow to 0.7 m in the vicinity of Cat Island, while in the back barrier of Ship and Horn Islands, waves can grow in excess of 1 m. These waves pass near the inlets and recurved spits, and as a result activate spit platforms, and adjacent shallow water in the vicinity of the recurved spits (Figure 7).

Model Evaluation

Tidal Model – Barataria Basin

The model was validated with field data using eight USGS stations within the basin. The station coverage extends from Barataria Pass, at the seaward entrance of the Basin, to Lake Cataouatche in the upper basin. An ordinary least squares harmonic analysis with robust fitting was applied to a yearlong time series of water level data from the field stations. The robust fitting extension minimizes the effects of storms or seasonal discharge variations and improves the overall accuracy of the results. The six principal tidal constituents from the field data are O1, K1, P1, M2, S2, and N2 (Figure 8). These constituents were selected because they were those chosen to force water levels at the ocean open boundary during the validation simulations (with the exception of P1, which was not resolved). Finally, a nodal correction was applied to the field data to correct for the amplitude variations associated with the 18.6 year nodal cycle. For evaluating the model's ability to reproduce tidal propagation up-basin, a 28 day period was selected in August 2007. This period was selected because in addition to tidal elevations throughout the basin, flow measurements and velocity distribution across the inlets was also available (FitzGerald et al, 2007). For this period, a harmonic analysis was performed on a 28-day record of model-simulated water levels at selected model nodes corresponding to the eight stations, and compared with field results (Table 4, Figure 8).

Figure 8 shows that the Basin is dominated by the principal lunar and lunisolar constituents, O1 and K1. These constituents can account for most of the astronomical variations in the Basin and were, thus the focus of the validation (Georgiou et al, 2010). Once these constituents were reproduced in the model, which was achieved through variation of the roughness height in the quadratic friction term of the bottom friction coefficient, no further adjustment was carried out. The validation was considered satisfactory despite the small disagreements in the principal lunar constituent M2, which in this area is only 8 % of the principal lunar, or of the order of 1 cm. Figure 8 shows scatter plots of observed versus simulated constituents for all locations where harmonic analysis was conducted. The model resolved and reproduced the propagation of the O1 and K1 constituents within 5 mm for almost all locations.

Table 4 Observed and simulated tidal constituents during model validation (values are in meters)

Site	S2	M2	N2	K1	O1
Barataria Pass (model)	0.005	0.010	0.002	0.117	0.117
Barataria Pass (obs)	0.008	0.018	0.006	0.121	0.118
North Grande Terre (model)	0.003	0.007	0.002	0.110	0.112
North Grande Terre (obs)	0.005	0.009	0.003	0.111	0.109
Barataria Bay North (model)	0.003	0.008	0.002	0.110	0.114
Barataria Bay North (obs)	0.005	0.007	0.003	0.109	0.107
Hackberry Bay (model)	0.001	0.005	0.001	0.072	0.070
Hackberry Bay (obs)	0.004	0.006	0.002	0.097	0.096
Barataria Waterway (model)	0.001	0.003	0.001	0.081	0.084
Barataria Waterway (obs)	0.003	0.006	0.002	0.080	0.079
Bay Dos Gris (model)	0.001	0.003	0.000	0.059	0.058
Bay Dos Gris (obs)	0.001	0.003	0.001	0.052	0.054
Little Lake (Cutoff) (model)	0.002	0.002	0.001	0.052	0.053
Little Lake (Cutoff) (obs)	0.001	0.002	0.001	0.044	0.051
Lake Cataouatche (model)	0.001	0.002	0.001	0.026	0.025
Lake Cataouatche (obs)	0.001	0.001	0.001	0.011	0.013

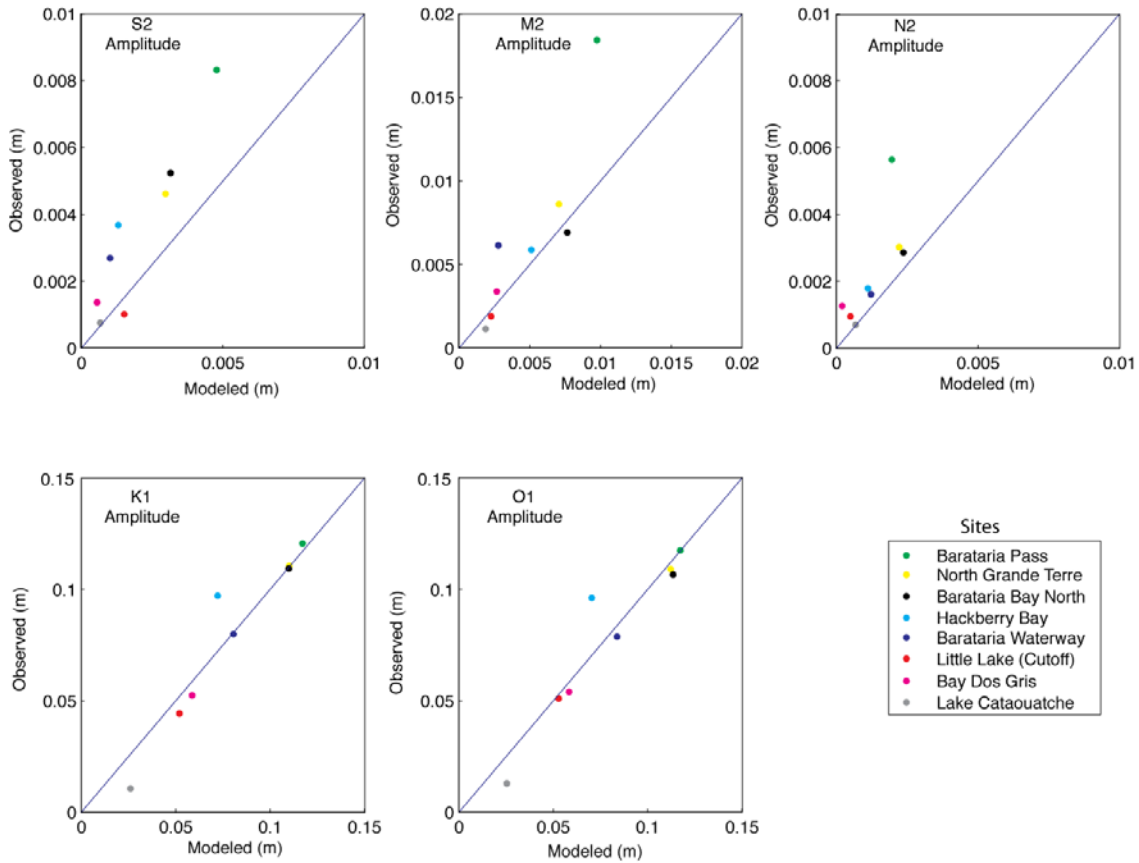


Figure 8 Graphical comparison of model simulated constituents with observations obtained from harmonic analysis during the validation period for August 2007.

Tidal Models – Pontchartrain, Mississippi and Breton Sound

Eleven stations with tides and/or salinity data were chosen for calibration, including stations in the upper Pontchartrain Estuary, tidal and navigation channels, and open water stations (Figure 6). These stations are operated by NOAA, USGS, NOAA PORTS, LUMCON, and USACE River gages. The D1 and D2 field data from this study were also used for model calibration. Table 5 lists the names of stations used, their identification numbers as designated by the operating agency, and the name of the operating agency. This table also specifies whether each station was used to calibrate tides (i.e., tidal amplitude and phase) or both tides and salinity.

The model was calibrated to reproduce observed tidal amplitude and phase variations at selected locations in the NGOM domain.

Salinity was also calibrated within the region, but to a less significant degree. The use of interpolated average annual values for initial salinity conditions, instead of observed data for the simulated time period, made it difficult to replicate observed salinities in the model. A lack of stations with salinity data during the period of interest prevented a more accurate initial salinity interpolation from being used in this project. Therefore, calibration efforts for salinity concentrated on reproducing reasonable salinity trends over the entire domain. For salinity calibration, adjustments of salinity magnitude were applied to observed station data to account for differences in sensor height. For instance, at D1, the salinity sensor was 0.4 m above the bottom of the bed, thereby representing bottom salinity. However, surface salinity results from the model were used for calibration. The adjustment applied accounts for the salinity gradient through the water column.

The calibration simulations were driven with meteorological and tide conditions from 3/31/10 to 4/22/10. During the calibration/validation process, efforts concentrated on calibrating the previously mentioned stations (shown in Figure 9) during the period of 4/16/10 to 4/22/10. This period was chosen for its relatively low winds and barometric pressure (Figure 10). By choosing a period with limited meteorological influences, the model's tidal calibration was conducted with more accuracy and confidence. It has been documented that the estuarine response to wind produces stronger circulation currents and setup than those produced by tidal motion (Georgiou & McCorquodale, 2002). Additionally, the passing of a seasonal front is accompanied by a high or low-pressure system that causes changes in barometric pressure. This change in atmospheric pressure greatly influences the water level in the vicinity of the front.

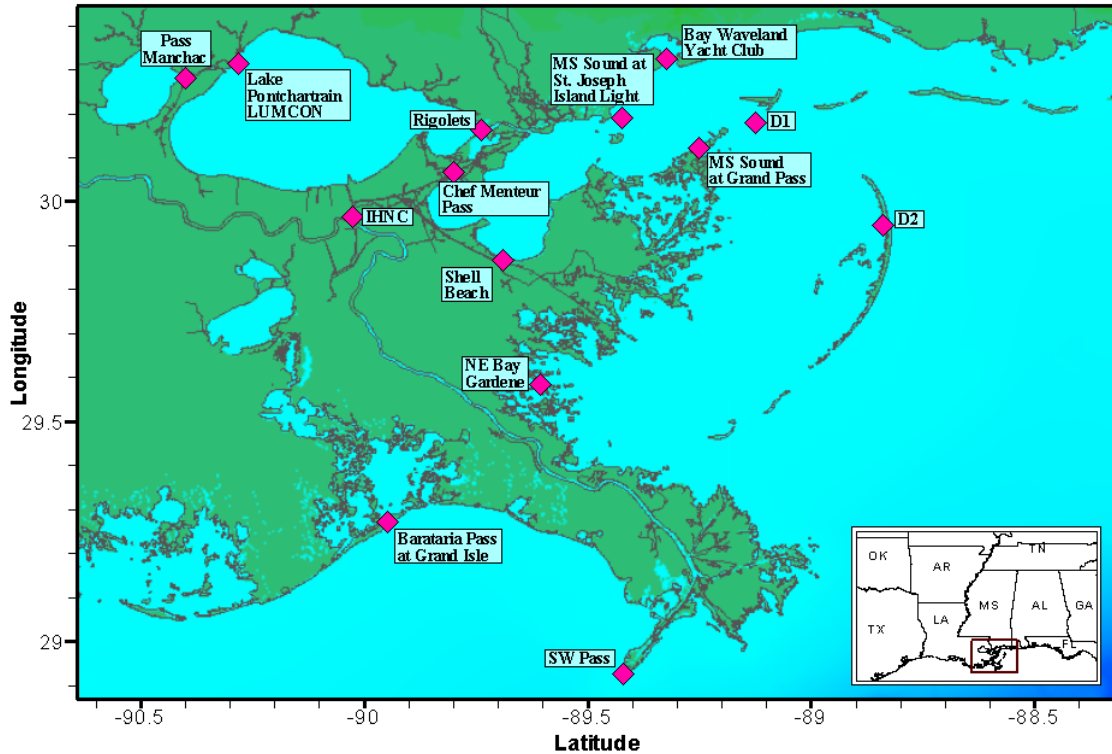


Figure 9 The inset shows a map of the states surrounding the northern Gulf of Mexico, while the red box outlines the area shown in the large image. The large image is a map of the calibration stations within the domain. Table 3 describes these stations in more

Table 5 - Stations used for model calibration. Station name, number, and operating agency, as well as calibration parameter are provided. Station numbers are in parentheses after station name.

Station	Agency	Calibration Type
Lake Pontchartrain LUMCON (103)	LUMCON	Tides, Salinity
IHNC (76160)	USACE Rivergages	Tides
Pass Manchac near Ponchatoula (85420)	USACE Rivergages	Tides
MS Sound at Grand Pass (300722089150100)	USGS	Tides, Salinity
Shell Beach (8761305)	NOAA	Tides
NE Bay Gardene near Point à la Hache (07374527)	USGS	Tides, Salinity
Rigolets near Lake Pontchartrain (85700)	USACE Rivergages	Tides, Salinity
Chef Menteur Pass near Lake Borgne (85750)	USACE Rivergages	Tides
Barataria Pass at Grand Isle (073802516)	USGS	Tides
Pilots Station East, SW Pass (8760922)	NOAA	Tides
Bay Waveland Yacht Club (8747437)	NOAA	Tides
MS Sound at St Joseph Island Light (301104089253400)	USGS	Tides, Salinity
D1	UNO	Tides, Salinity
D2	UNO	Tides, Salinity

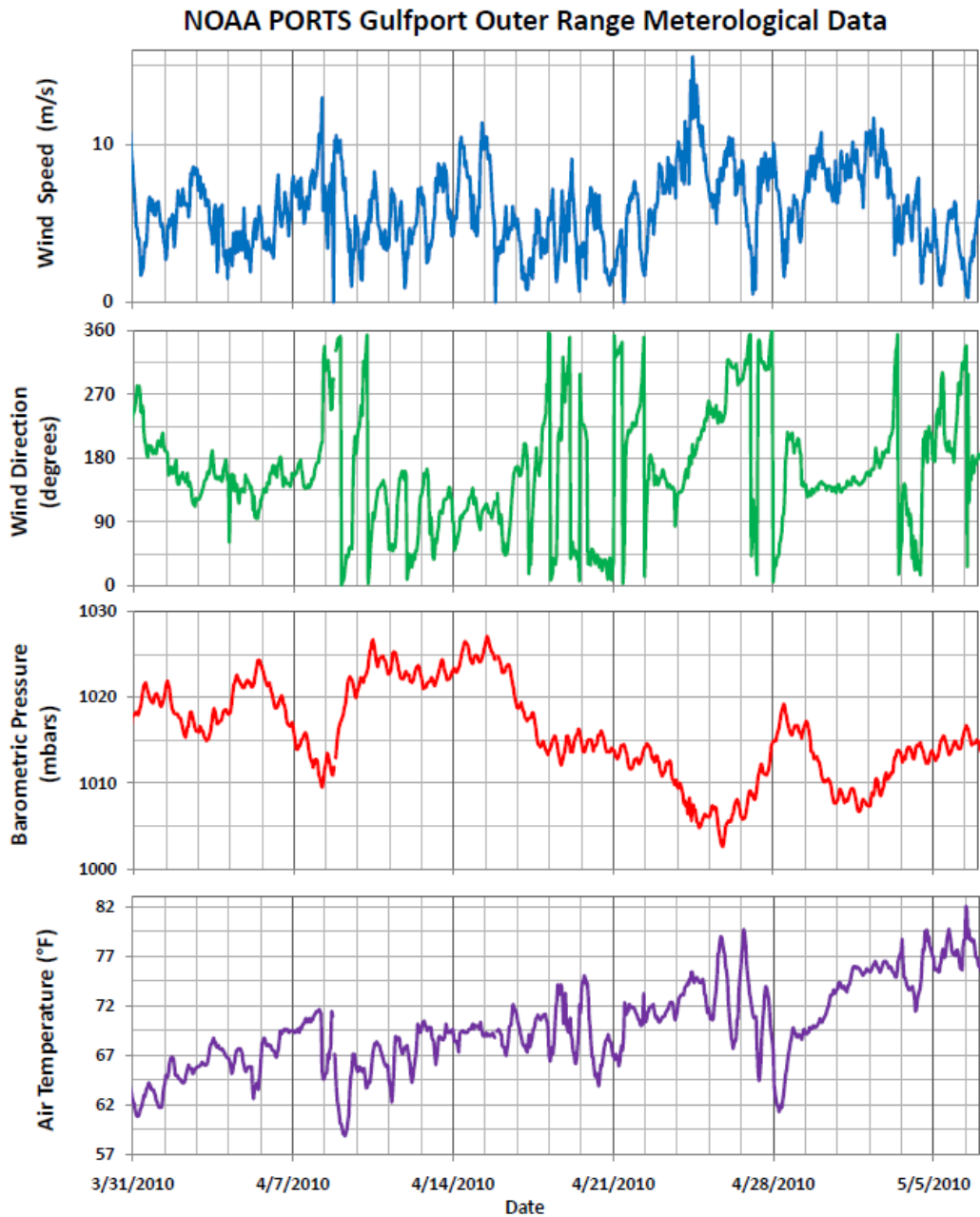


Figure 10 - Meteorological conditions at the NOAA NOS Gulfport Outer Range station (Station GPOM6 – 8744707) for the period of 3/31/10 to 5/7/10.

Bottom roughness (z_{0b}) were adjusted during the calibration phase to correct inland tidal propagation and attenuation (Schindler 2010). For instance, when tidal amplitudes were represented accurately at Grand Pass but under-represented at Pass Manchac, the bottom roughness was reduced. By reducing the bottom roughness, tidal amplitudes were less

dampened. Simulations were conducted with bottom roughness hof 0.0013 m, 0.0011 m, and 0.0009 m; a bottom roughness of 0.0009 m produced the most accurate results.

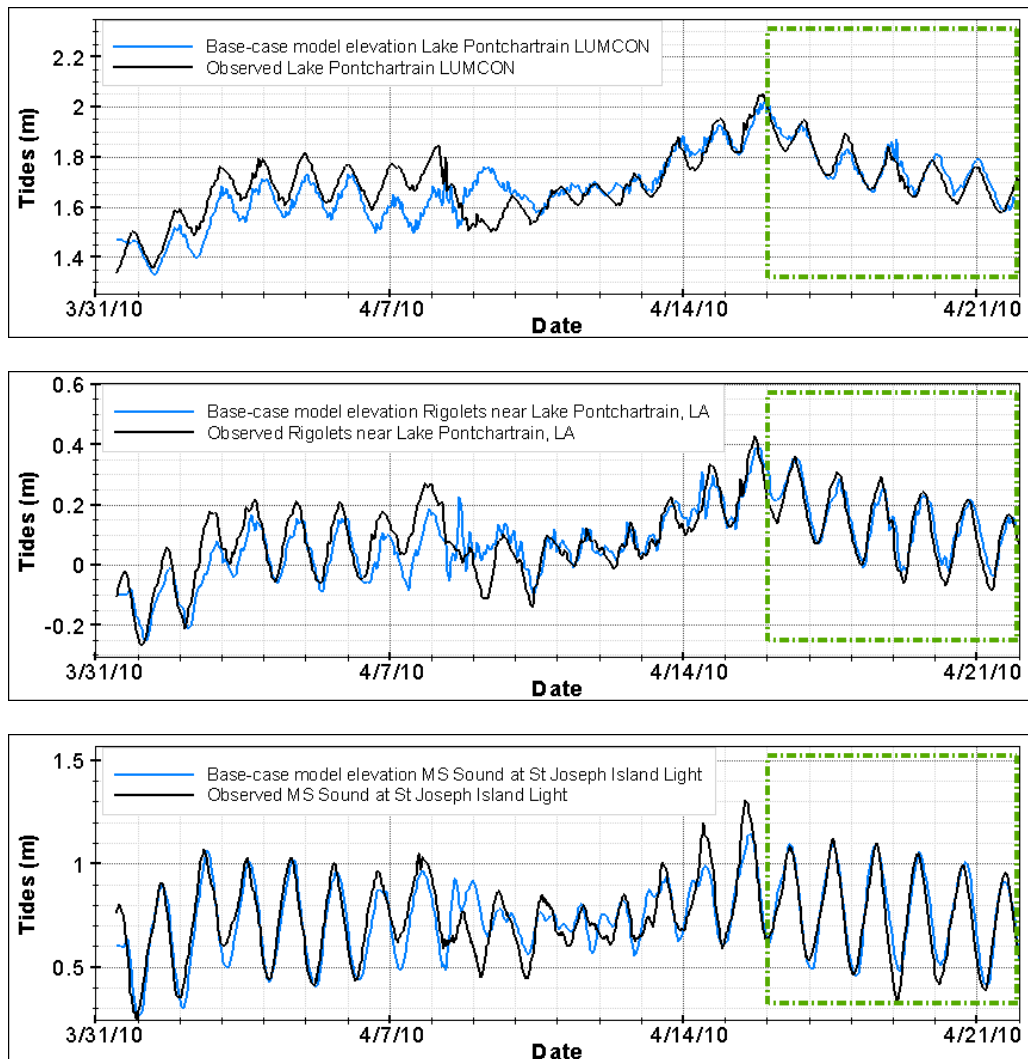


Figure 11 – Comparison of base-case scenario tides (meters) and observed tide data for the calibration period (3/31/10 to 4/22/10). Calibration efforts focused on good correlation during the period of 4/16/10 to 4/22/10 (inside the green box) at the following locations (from top to bottom): Lake Pontchartrain at LUMCON, Rigolets near Lake Pontchartrain, and Mississippi Sound at St. Joseph Island Light. An adjustment was applied to observed data to account for vertical datum differences.

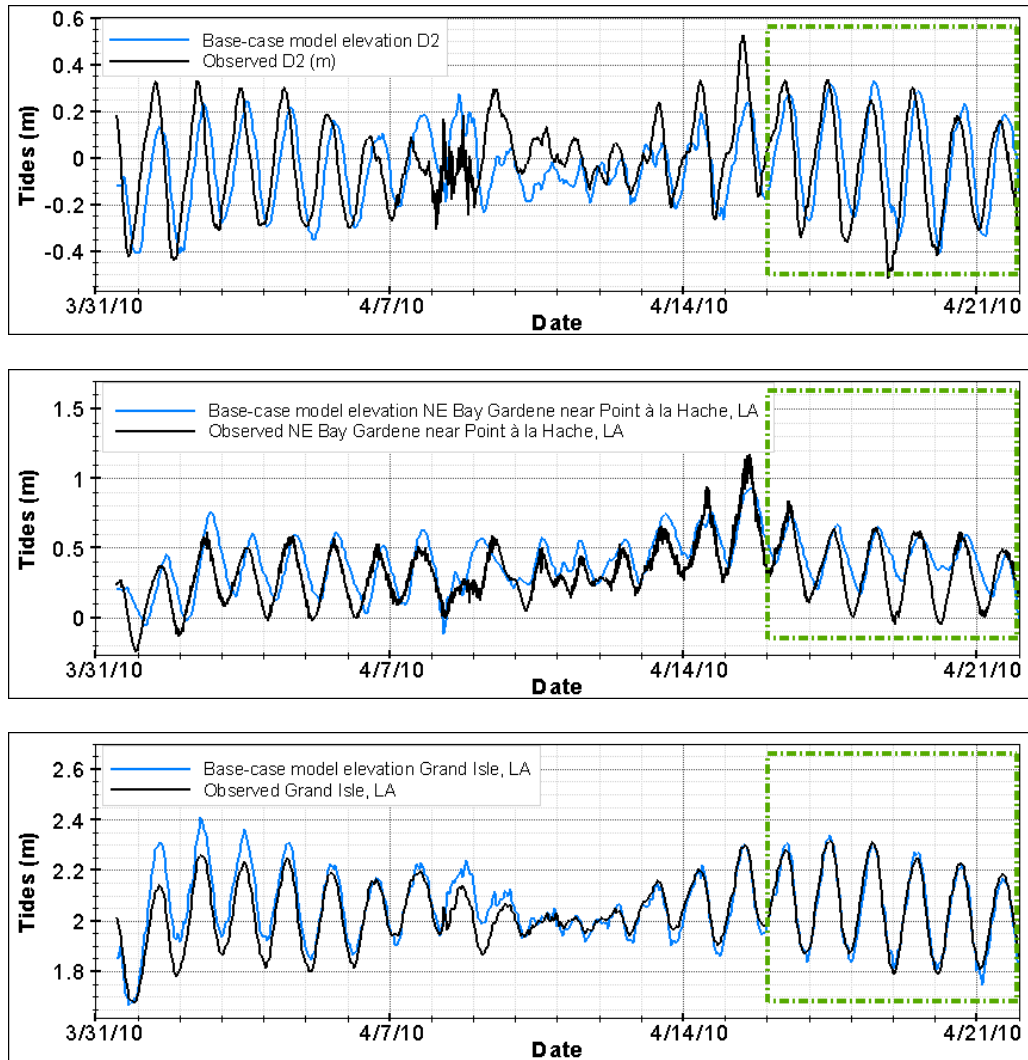


Figure 12 - Comparison of base-case scenario tides (meters) and observed tide data for the calibration period (3/31/10 to 4/22/10). Calibration efforts focused on good correlation during the period of 4/16/10 to 4/22/10 (inside the green box) at the locations (from top to bottom): D2, NE Bay Gardene near Point à la Hache and Barataria Pass at Grand Isle. An adjustment was applied to observed data to account for vertical datum differences.

Figure 11 and Figure 12 show that the model replicated the tidal amplitude within a maximum range of approximately 13 cm (reinforced by the results shown in Table 6). Results were generally in-phase, with the largest phase deviations at shallow nodes (such as NE Bay Gardene and D2). Accurate bathymetry in these areas was unavailable at the time of grid generation, and it is believed that local discrepancies in bathymetry are the cause of the larger phase and amplitude disparity at these sites. The Lake Pontchartrain stations replicated phase well, but underestimated amplitude during the beginning of the period. The good phase correlation indicates that the problem is not due to tidal attenuation near the interior domain (a common

problem in a domain as large as this, but resolved during the calibration phase). It is believed that these differences in amplitude result from corresponding changes in barometric pressure. FVCOM does not account for changes in atmospheric pressure, and therefore produces tidal elevations resulting from wind and astronomical tides only. The aforementioned stations do replicate tidal signatures during normal periods well (a difference of less than 10 cm), however all stations poorly simulate the tidal conditions (both phase and amplitude) around the dates of 4/8/10 to 4/9/10. A cold front passed through the area during this time, producing strong northerly winds and drastic changes in barometric pressures (See Figure 10).

For a numerical comparison of these signals, mean absolute error (MAE) and root-mean-square error (RMSE) were computed. The MAE was calculated with the equation:

$$MAE = \frac{\sum_{i=1}^n |X_{obs} - X_{sim}|}{n} \quad (18)$$

where X_{obs} and X_{sim} represent the observed and simulated data points and n is the number of data points. The RMSE was computed as

$$RMSE = \sqrt{\frac{\sum_{i=1}^n (X_{obs} - X_{sim})^2}{n}} \quad (19)$$

The range of the observed data provides an important gauge for determining the degree of error. Smaller ratios of MAE to range indicate that the simulated data has a small degree of deviation from the observed data. The range is calculated by subtracting the minimum value ($X_{obs,min}$) from the maximum value ($X_{obs,max}$) of each observed dataset.

$$Range = X_{obs,max} - X_{obs,min} \quad (20)$$

These values, calculated for the period of 4/16/2010 to 4/22/2010, provide a mathematical assessment of the base-case scenario validation. Table 6 lists each station and its corresponding tidal MAE and RMSE values in ascending order of error. The highest tidal MAE and RMSE rates (Shell Beach to D2 in Table 4) are found at stations where recent bathymetric data were unavailable and bathymetries had to be estimated for the mesh. Considering this fact, and the fact that model results will be used to determine trends not magnitudes, the errors at these stations are within a reasonable range. Stations with recent bathymetries and less complex topographies (interior domain and channels) had lower error values.

Table 6 – MAE and RMSE values (in meters) at each tidal calibration station during the period of 4/16/10 to 4/22/10. Stations are shown in ascending order of error.

Station	Tidal MAE	Tidal RMSE	Range (m)
Rigolets	0.0422	0.0520	0.5090
LUMCON	0.0435	0.0592	0.4650
MS Sound at St Joseph Island Light	0.0475	0.0620	0.7803
Pass Manchac	0.0479	0.0643	0.4328
SW Pass, LA	0.0576	0.0693	0.5883
Barataria Pass at Grand Isle	0.0599	0.0765	0.6736
IHNC	0.0621	0.0732	0.5791
Chef Menteur	0.0630	0.0775	0.5761
Shell Beach	0.0790	0.0954	0.6462
MS Sound at Grand Pass	0.0895	0.1100	0.6797
Bay Waveland Yacht Club	0.1092	0.1328	0.8595
D1	0.1180	0.1427	0.9508
NE Bay Gardene	0.1358	0.1717	0.8595
D2	0.1374	0.1627	0.8467

Wave Model

Two directional CSI wave buoys (CSI 16 and CSI 9; Coastal Studies Institute, WAVCIS Program) lie within the domain for the OSAT3 model (Figure 1). There are no available NOAA buoys within our model domain – most of the NOAA buoys are in deeper water outside our domain. We evaluated model skill by comparing over similar stationary conditions, waves predicted by the model with observations at these two CSI locations. The results from the wave model skill are graphically shown in Figure 13 and Figure 14. Generally, in Barataria bight, Breton and Chandeleur sound (CSI 16; Figure 14) the model is reproducing waves very well. Although the agreement between model and observations is fair for the western portion of the domain (near Timbalier Islands) the performance of the model is still acceptable, given uncertainties in the bathymetry, and the fact that this station exhibits higher variance in the observations (error bars in the plots).

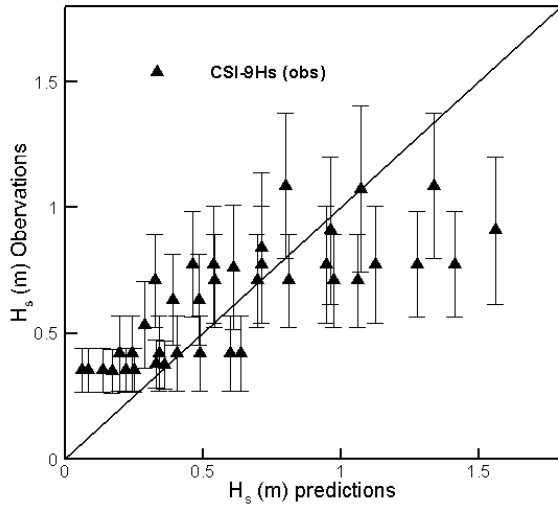


Figure 13 Wave model skill showing significant wave height comparison at station CSI 9

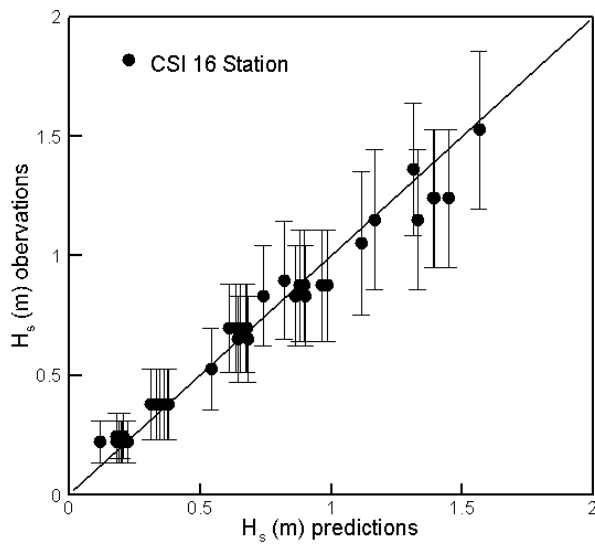


Figure 14 Wave model skill showing significant wave height comparison at station CSI 16

Summary and Concluding remarks

The authors have developed a SWAN model and used tidal models to assess potential transport of sediment and SRBs within the study area of Louisiana and Mississippi using semi-empirical equations. We have provided a model-based assessment of transport and deposition of residual oil that is causing, or presumed to be causing, shoreline re-oiling within the northern Gulf of

Mexico in the form of mixtures of sand and weathered oil, known as surface residual balls (SRBs). Our results show spatial variations in alongshore rms-currents, including locations where these gradients result in convergence or divergent zones, areas that will likely accumulate SRBs if they are in the vicinity. Model results also showed that spit platforms, recurved spits, and other shallow environments in the vicinity of barrier islands, can be fairly active environments, and will likely remain as such until nearby sources of SRBs are diminished. In addition, model results also confirmed that offshore winds, given fetch in excess of 20 km can generate waves that can reach 0.5 – 1 m in height, which further create active transport along re-curved spits, and spit platforms. As a result, these environments may either naturally accumulate SRBs (if a source is present updrift), and are likely to experience burial of material that is already there (having arrived from a previous transport event). Finally, our model results identify spatial and temporal variations in the mobility of sand and SRBs.

Modeling results suggest that, under the most commonly observed low-energy wave conditions, larger SRBs are not likely to move very far alongshore, suggesting small redistribution of larger SRBs during non-storm conditions. Under storm conditions, however, it is possible for larger SRBs to be mobilized. However, lag effects and transient energy conditions, as well as normal conditions, can cause larger SRBs to be either buried, or unburied. This is possible in part due to the fact that large SRBs are less mobile than sand, which creates additional complexities in accurately modeling their behavior. In addition to complexities created by lag effects and transient energy conditions, at large size classes (for instance SRBs of 10 cm) the transport algorithms have lower performance because limited datasets exist to validate the predictions.

References

Battjes, J.A., and Janssen, J.P.F.M., 1978, Energy loss and set-up due to breaking of random waves, chap. 32 of Coastal engineering—1978: [Conference on Coastal Engineering, 16th, Hamburg, Germany, 1978](#), Proceedings, p. 569–587.

- Booij, N., Ris, R.C., and Holthuijsen, L.H., 1999, A third-generation wave model for coastal regions—1. Model description and validation: *Journal of Geophysical Research*, v. 104, no. C4, p. 7649–7666.
- Bottacin-Busolin, Andrea, Tait, Simon, Marion, Andrea, Chegini, Amir, and Tregnaghi, Matteo, 2008, Probabilistic description of grain resistance from simultaneous flow field and grain motion measurements: *Water Resources Research*, v. 44, no. 9, WO9419, 12 p.
- Boyer, D.L., Fernando, H.J.S., and Voropayev, S.I., 2002, The dynamics of cobbles in and near the surf zone: Arizona State University, 37 p., accessed September 5, 2012, at <http://www.dtic.mil/dtic/tr/fulltext/u2/a412197.pdf>.
- Burchard, H., 2002. Applied turbulence modeling in marine waters. *Springer:Berlin-Heidelberg-New York-Barcelona-Hong Kong-London-Milan Paris-Tokyo*, 215pp.
- Chen, C. H. Liu, R. C. Beardsley, 2003. An unstructured, finite-volume, three-dimensional, primitive equation ocean model: application to coastal ocean and estuaries. *J. Atm. & Oceanic Tech.*, 20, 159-186.
- Davies, A.G., Soulsby, R.L., and King, H.L., 1988, A numerical model of the combined wave and current bottom boundary layer: *Journal of Geophysical Research—Oceans*, v. 93, no. C1, January 15, p. 491–508.
- FitzGerald, D., Howes, N., Kulp, M., Hughes, Z., **Georgiou, I.Y.**, and Penland, S., 2007, Impacts of rising sea level to backbarrier wetlands, tidal inlets, and barriers: Barataria Coast, Louisiana, Coastal Sediments 07, Conference Proceedings, CD-ROM13.
- Georgiou, I.Y., McCorquodale, J. A., Schindler, J., Retana A.G., FitzGerald, D.M., Hughes, Z., Howes, N., 2009, Impact of Multiple Freshwater Diversions on the Salinity Distribution in the Pontchartrain Estuary under Tidal Forcing, *Journal of Coastal Research*, Vol. 54, pp. 59 – 70.
- Georgiou, I.Y., McCorquodale, J.A., Nepani, J., Howes, N., Hughes, Z., FitzGerald, D.M., Schindler, J.K., 2010, Modeling the hydrodynamics of diversions into Barataria Bay, Technical Final Report submitted to the Lake Pontchartrain Basin Foundation, Pontchartrain Institute for Environmental Sciences, March 2010, New Orleans, LA 70148, 82 pp.

- Hasselmann, K., Barnett, T.P., Bouws, E., Carlson, H., Cartwright, D.E., Enke, K., Ewing, J.A., Gienapp, H., Hassellman, D.E., Kruseman, P., Meerburg, A., Müller, P., Olbers, D.J., Richter, K., Sell, W., and Walden, H., 1973, Measurements of wind-wave growth and swell decay during the joint North Sea wave project (JONSWAP): Hamburg, Germany, Deutsches Hydrographisches Institut Ergänzungsheft zur Deutschen Hydrographischen Zeitschrift Reihe A, v. 8, no. 12, 95 p., accessed September 5, 2012, at ftp://ftp.ifremer.fr/ifremer/cersat/products/gridded/wavewatch3/pub/WAVE_PAPERS/Hasselmann_etal_DHZ1973.pdf.
- Komen, G.J., Hasselmann, S., and Hasselmann, K., 1984, On the existence of a fully developed wind-sea spectrum: *Journal of Physical Oceanography*, v. 14, no. 8, p. 1271–1285.
- Lesser, G.R., Roelvink, J.A., van Kester, J.A.T.M., and Stelling, G.S., 2004, Development and validation of a three-dimensional morphological model: *Journal of Coastal Engineering*, v. 51, nos. 8–9, October, p. 883–915.
- Love, M.R., Amante, C.J., Eakins, B.W., and Taylor, L.A., 2012, Digital elevation models of the northern Gulf coast—Procedures, data sources and analysis: National Oceanic and Atmospheric Administration Technical Memorandum NESDIS NGDC–59, 43 p., accessed September 5, 2012, at <http://www.ngdc.noaa.gov/dem/squareCellGrid/download/731>.
- Li, C, N., Walker, A., Hou, J., Georgiou I.Y., H., Roberts, E., Laws, E., Weeks, X., Li, J., Crochet. 2008. Circular Plumes in Lake Pontchartrain under Wind Straining, *Estuarine Coastal and Shelf Science*, v. 80, iss. 1, p. 161-172.
- Mellor, G. L. and T. Yamada, 1982, Development of a turbulence closure model for geophysical fluid problem. *Rev. Geophys. Space. Phys.*, 20, 851-875.
- National Oceanic and Atmospheric Administration, [undated a], Center for Operational Oceanographic Products and Services—National Ocean Service tide stations, Pensacola Bay,

- FL (8729840),: National Oceanic and Atmospheric Administration, accessed September 5, 2012, at <http://tidesandcurrents.noaa.gov/index.shtml>.
- National Oceanic and Atmospheric Administration, [undated b], Digital coast—2010 U.S. Army Corps of Engineers topo/bathy lidar—Alabama and Florida: National Oceanic and Atmospheric Administration, accessed September 5, 2012, at <http://www.csc.noaa.gov/dataviewer/>.
- National Oceanic and Atmospheric Administration, [undated c], National Data Buoy Center— Meteorological/ocean stations 42040: National Oceanic and Atmospheric Administration, accessed September 5, 2012, at <http://www.ndbc.noaa.gov/>.
- Poirrier, M.A., 1979., Studies of stratification in southern Lake Pontchartrain near the Inner Harbor Navigational Canal. *Proceedings of the Louisiana Academy of Sciences*, 41:26-35
- Reniers, A.J.H.M., Thornton, E.B., Stanton, T.P., and Roelvink, J.A., 2004, Vertical flow structure during Sandy Duck—Observations and modeling: *Coastal Engineering*, v. 51, no. 3, p. 237–260.
- Ris, R.C., Holthuijsen, L.H., and Booij, N., 1999, A third-generation wave model for coastal regions—2. Verification: *Journal of Geophysical Research*, v. 104, no. C4, p. 7667–7681.
- Schindler, Jennifer, "Estuarine Dynamics as a Function of Barrier Island Transgression and Wetland Loss: Understanding the Transport and Exchange Processes" (2010). *University of New Orleans Theses and Dissertations*. Paper 1260.
- Soulsby, R.L., 1997, *Dynamics of marine sands—A manual for practical applications*: London, Thomas Telford Publications, 249 p.
- Soulsby, R.L., and Damgaard, J.S., 2005, Bedload sediment transport in coastal waters: *Coastal Engineering*, v. 52, no. 8, August, p. 673–689.